Electronic Supplementary Material (ESI) for Energy & Environmental Science.
This journal is © The Royal Society of Chemistry 2024

Supporting Information

Deciphering the dynamic interfacial chemistry of calcium metal anodes

Huijun Lin,[1] Jiayi Meng,[2] Weihua Guo,[3] Renjie Li,[1] Yuyang Yi,[1] Yiyuan Ma,[1] Chi Fai Cheung,[1] Doron Aurbach,[4] Zheng-Long Xu [1,5*]*

1. State Key Laboratory of Ultra-precision Machining Technology, Department of Industrial and Systems Engineering, The Hong Kong Polytechnic University, Hung Hom, Hong Kong, P.R. China.

2. Zhixing College, Beijing Normal University, Zhuhai, P.R. China.

3. Department of Chemistry, City University of Hong Kong, Hong Kong, P.R. China.

4. Department of Chemistry and BIU institute of advanced materials & nanotechnology, Bar-Ilan university, Ramat-Gan, Israel

5. Shenzhen Research Institute, The Hong Kong Polytechnic University, Shenzhen, P.R. China.

*Corresponding authors: doron.aurbach@biu.ac.il (D.A.) zhenglong.xu@polyu.edu.hk (Z.L.X.)

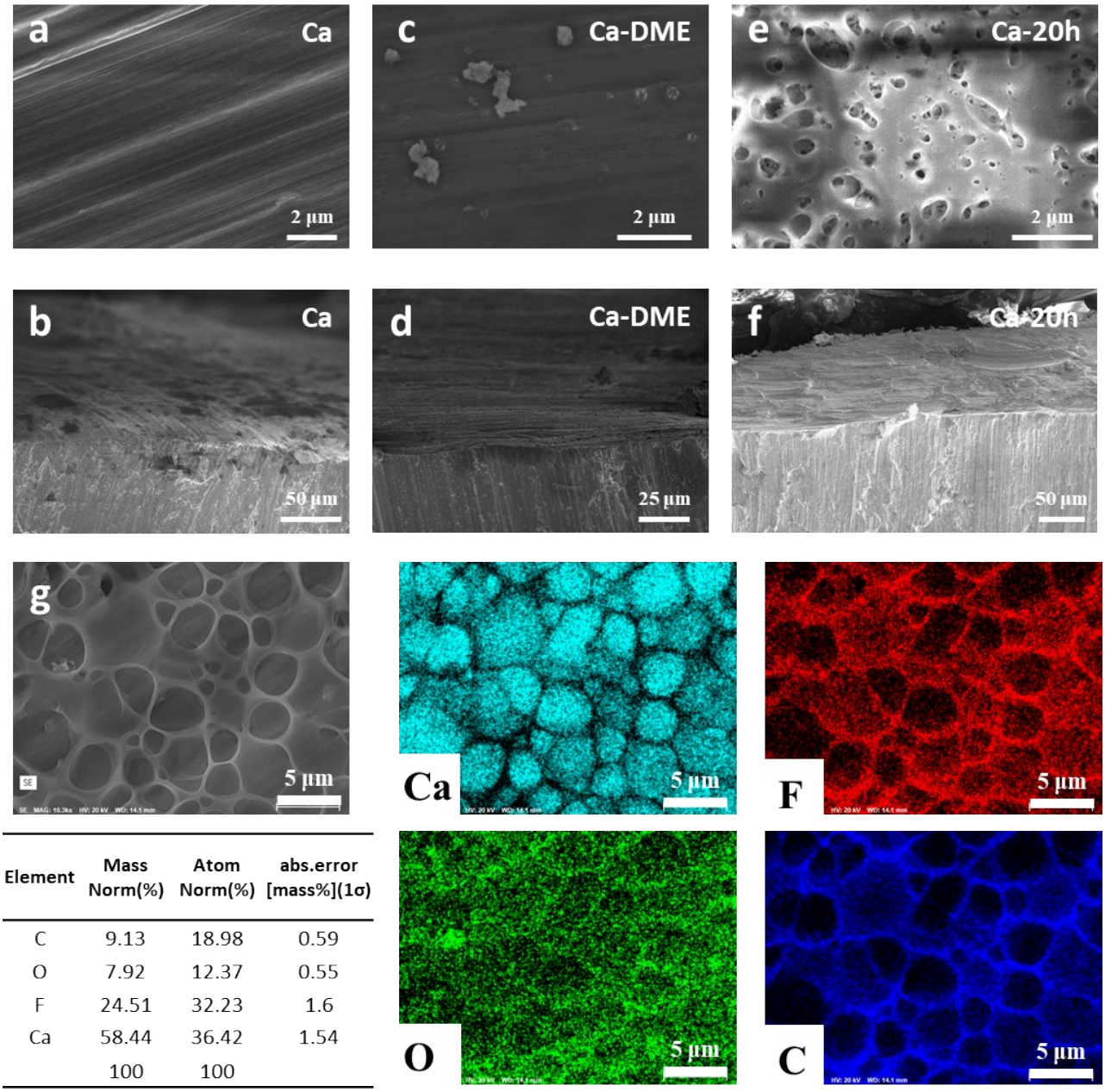

Element	Mass Norm(%)	Atom Norm(%)	abs.error [mass%](1σ)
C	9.13	18.98	0.59
O	7.92	12.37	0.55
F	24.51	32.23	1.6
Ca	58.44	36.42	1.54
	100	100	

Figure S1. Top-view and cross-sectional view SEM images of (a, b) pristine Ca, (c, d) Ca-DME and (e, f) Ca-20h. (g) High solution SEM image and EDS elemental mapping of Ca-20h electrode. It shows highly porous structure and abundant organic elements.

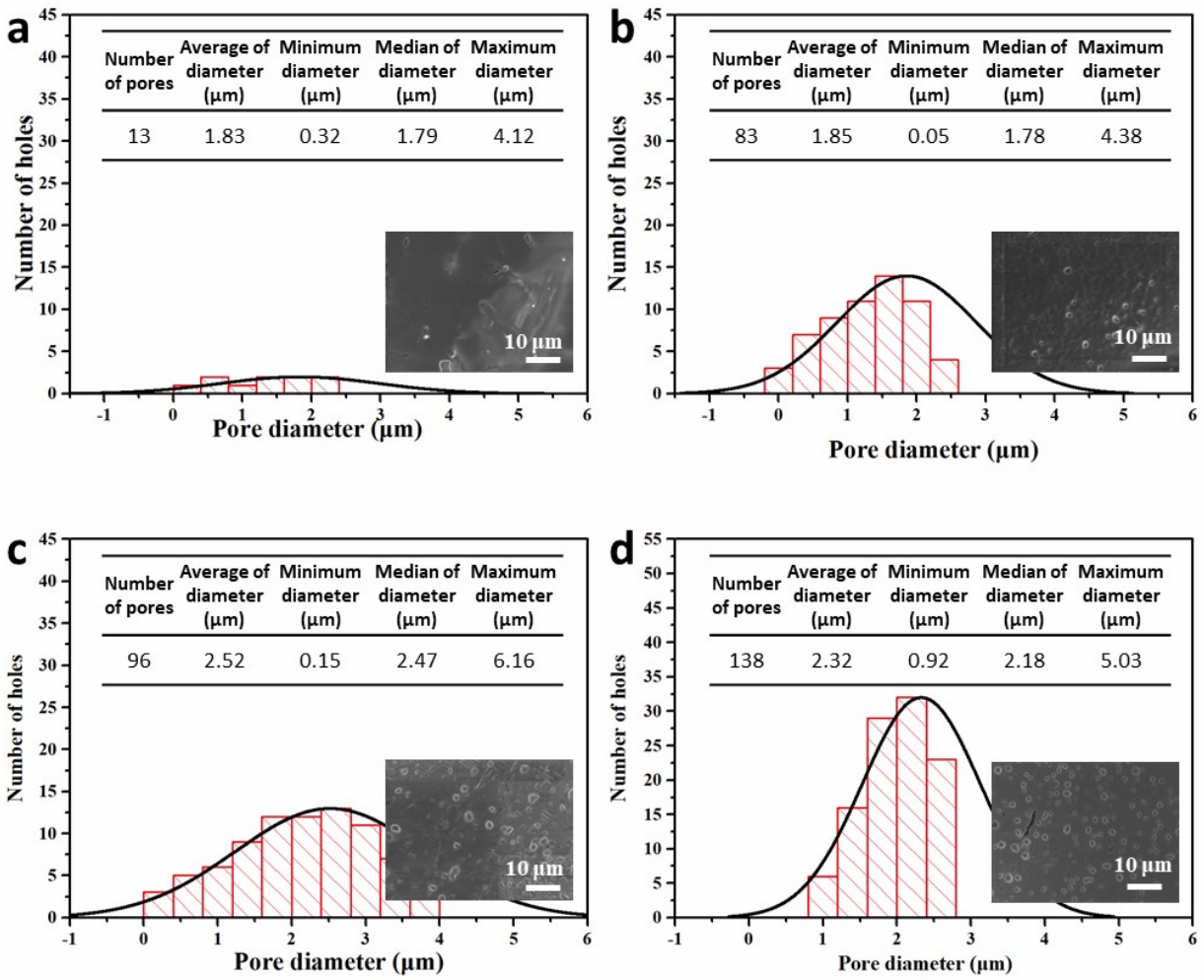

Figure S2. Statistical analysis of the pore size distributions on the surface of (a) Ca-1h, (b) Ca-5h, (c) Ca-20h, (d) Ca-40h.The average pore size increases from around 1.8 μm for Ca-1h and Ca-5h to 2.5 μm for Ca-20h, indicating continuous Ca metal corrosion in the $Ca[B(hfip)_4]_2$/DME electrolyte solution.

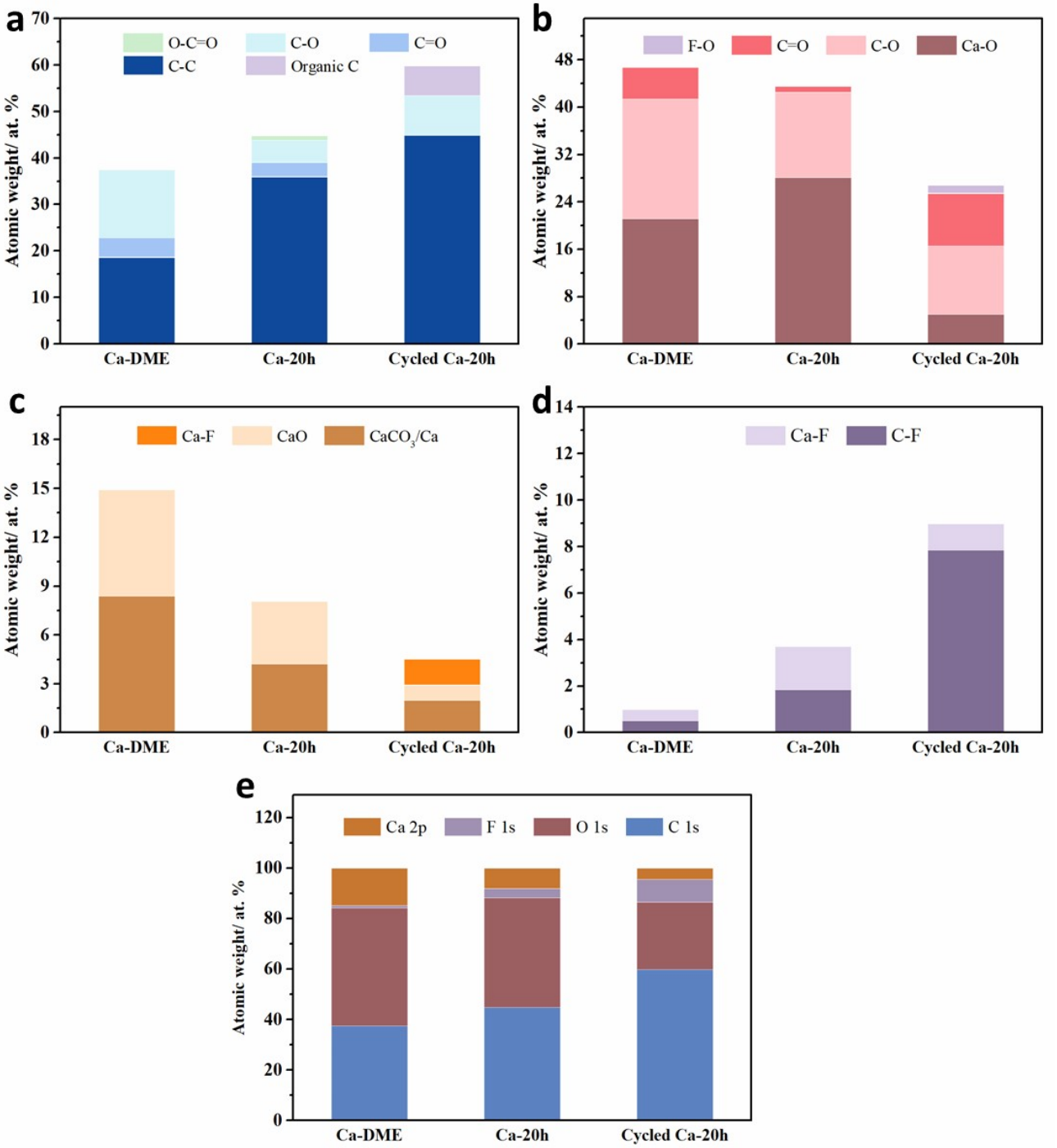

Figure S3. The deconvoluted peak intensities of XPS results in Fig. 1i, 1j and Fig. S9a: (a) C1s, (b) O 1s, (c) Ca 2p and (d) F 1s. (e) Atomic ratios in general XPS spectra of Ca-DME, Ca-20h and Ca-20h-CV electrodes. After soaking in electrolyte and CV cycling, the organic components (C-C/C=O/O-C=O/C-F) are largely increased, which are considered beneficial for Ca metal cycling.

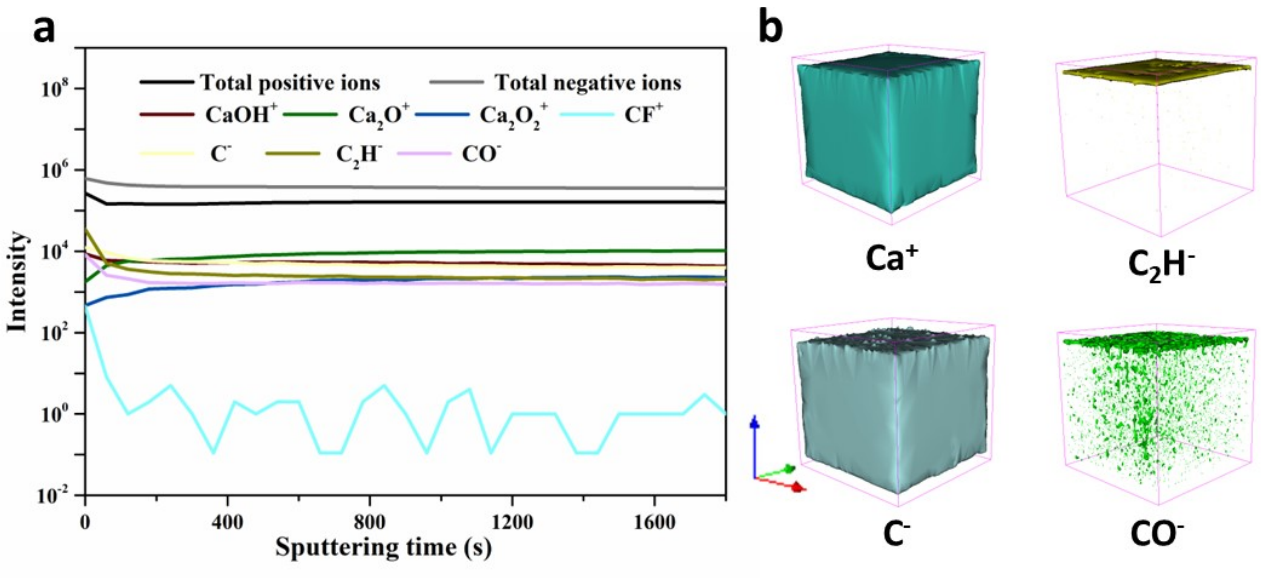

Figure S4. (a) TOF-SIMS fragments intensity evolution and (b) results of Ca-20h surface analysis.

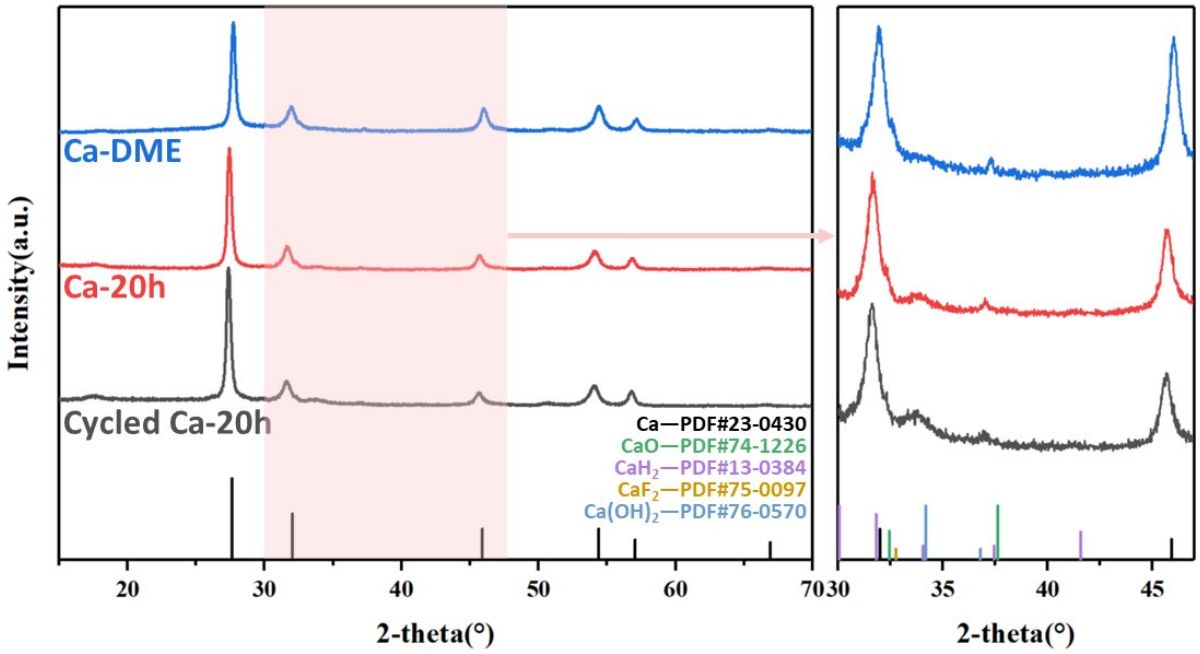

Figure S5. GIXRD patterns of Ca-DME, Ca-20h and cycled Ca-20h. The left shows dominant Ca metal patterns for the surface layer, and the augmented region in the right side presents marginal peaks referring to the CaH_2, CaO, and $Ca(OH)_2$ crystalline features.

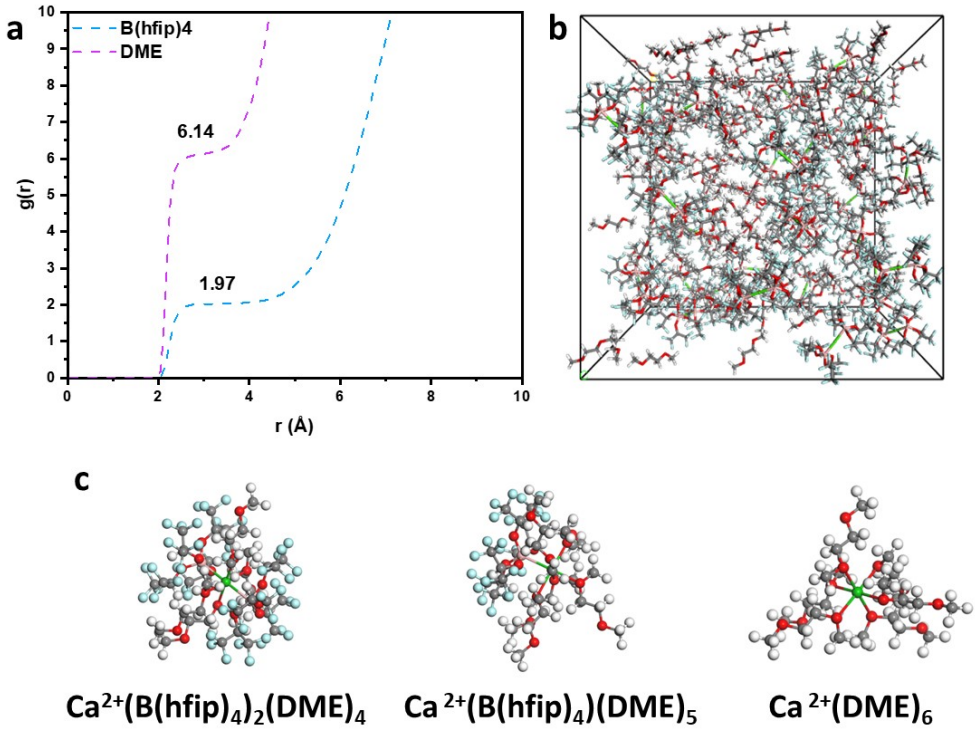

Figure S6. (a) Coordination number *g(r)* obtained from radial distribution functions. *r*, radial distance from Ca^{2+}. (b) Solvation structure and (c) snapshots of the dominant structures for the $Ca[B(hfip)_4]_2$/DME electrolyte solution.

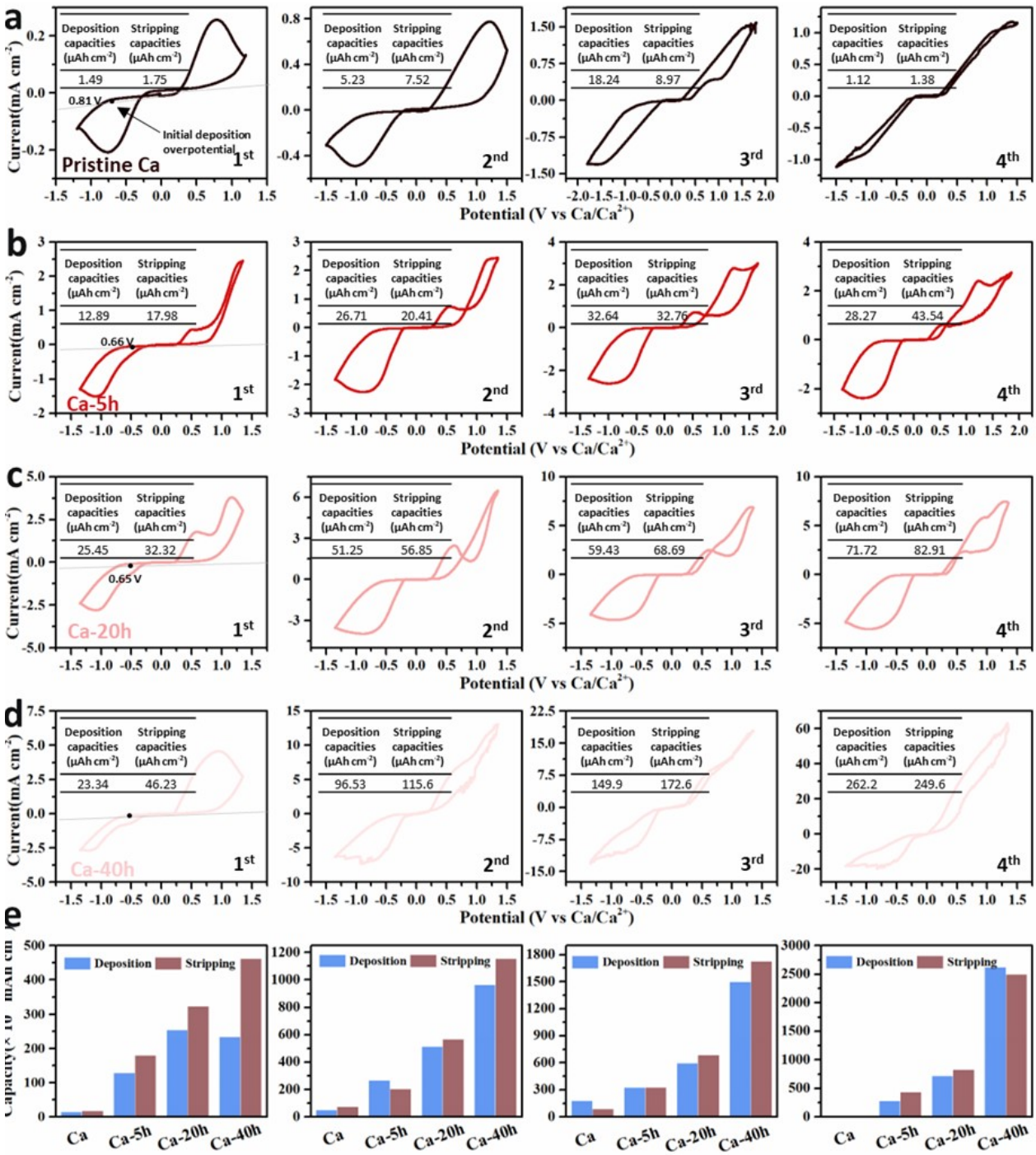

Figure S7. CV cycles of (a) Ca//Ca, (b) Ca-5h//Ca-5h, (c) Ca-20h//Ca-20h, and (d) Ca-40h//Ca-40h symmetric cells at a scan rate of 25 mV s^{-1} in 0.25 M $Ca[B(hfip)_4]_2$/DME electrolyte. (e) The calculated Ca metal deposition and stripping capacities in (a-d). Points in (a-d) show the initial deposition overpotentials for different Ca electrodes. The Ca platting/striping capacities are increasing with the chemical ageing time, suggesting increased activities of Ca metal during electrolyte soaking.

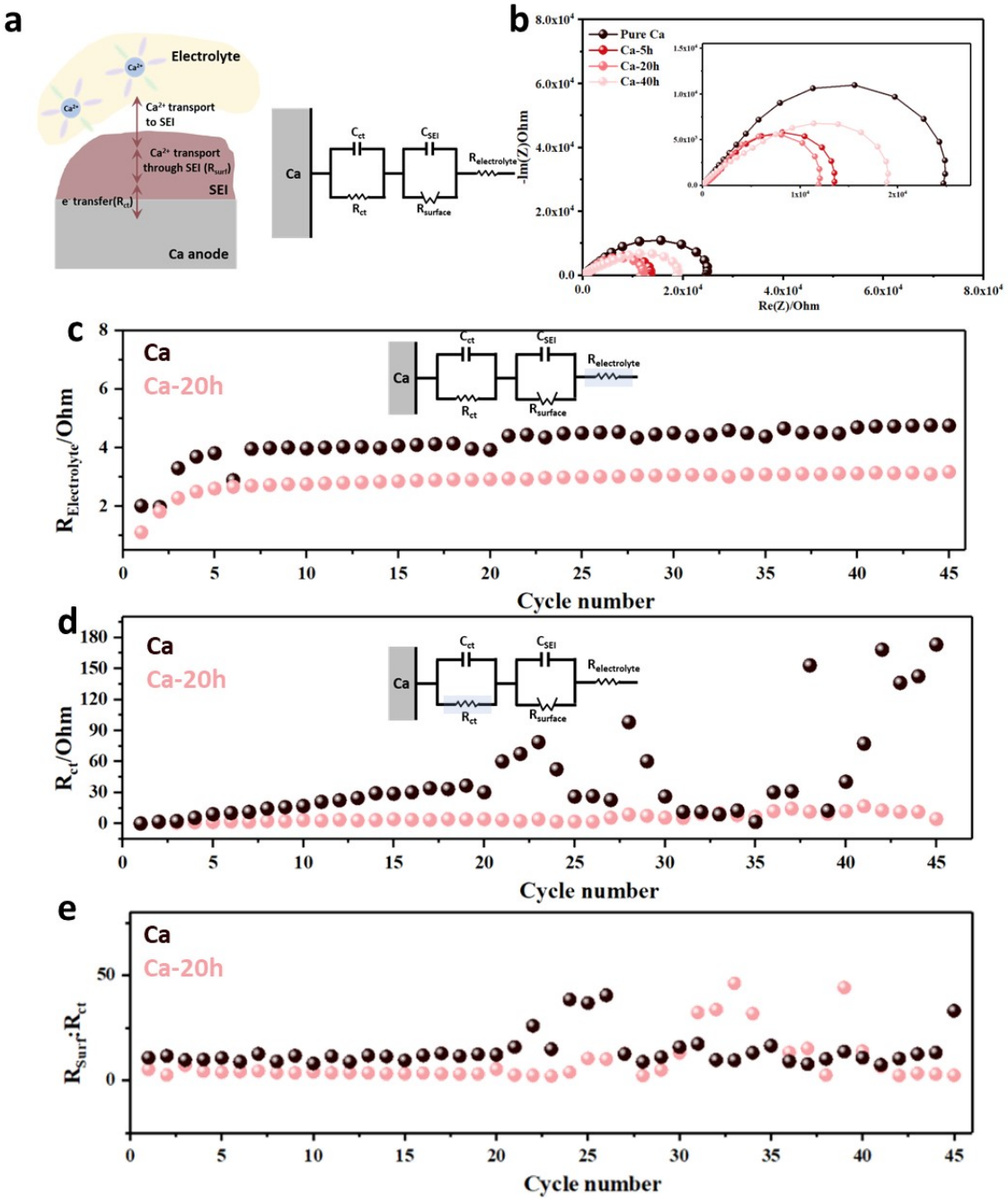

Figure S8. (a) Illustration of the charge transfer processes from the bulk electrolyte solution to the Ca metal electrode, and the equivalent circuit analogue to fit the EIS spectra presented as Nyquist plots.[1-3] (b) Impedance spectra of Ca//Ca, Ca-5h//Ca-5h, Ca-20h//Ca-20h and Ca-40h//Ca-40h fresh symmetric cells, the Ca-20h//Ca-20h presents the smallest impedance, indicative of the enhanced activation of Ca metal after electrolyte solution's soaking. The cycle number-sequential resistance values for Ca//Ca and Ca-20h//Ca-20h cells, including (c) $R_{Electrolyte}$, (d) R_{ct}, and (e) R_{surf}, where $R_{Electrolyte}$ is the electrolyte, diaphragm and other inherent impedance of the cell, R_{Surf} refers to the Ca ion diffusion through the SEI and the electrode/solution interface. (c-e) is plotted from the 1st cycle.

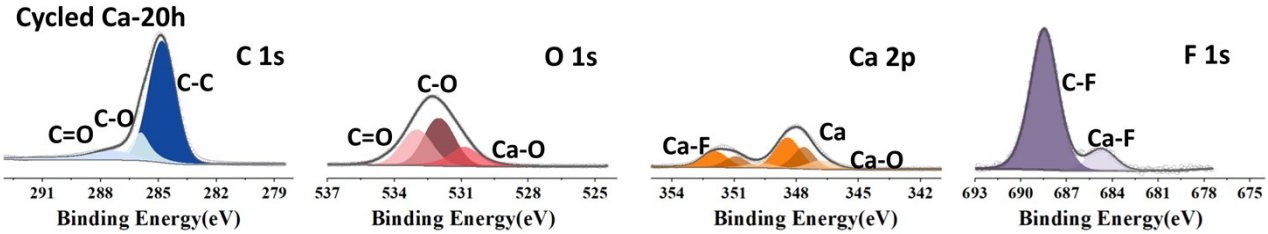

Figure S9. Deconvoluted C1s, O1s, Ca 2p, and F1s peaks in XPS of the Ca-20h electrode after CV cycling.

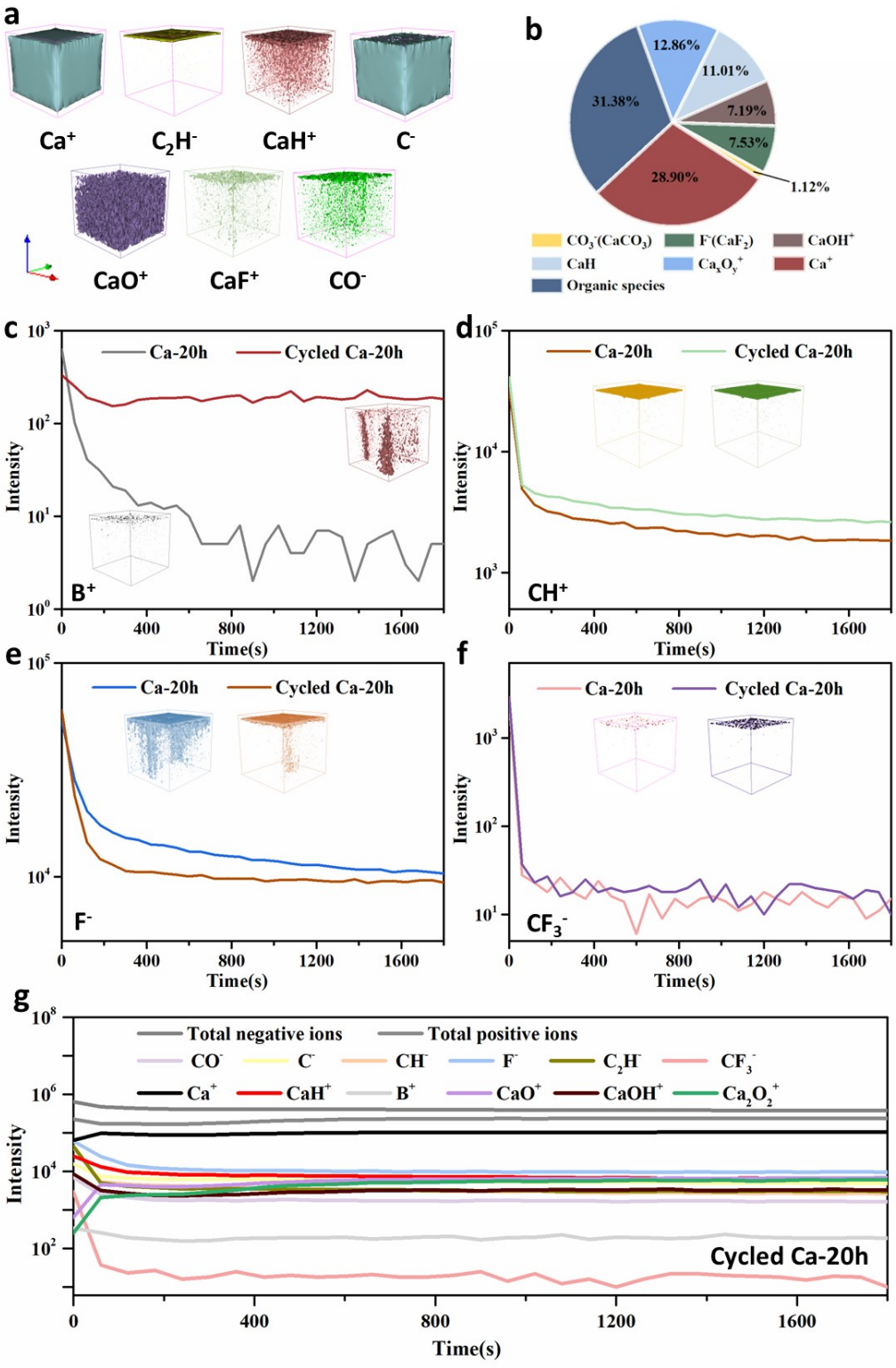

Figure S10. (a) TOF-SIMS fragments analysis of Ca-20h electrodes after CV cycling. (b) Statistics of surface (~10 nm) composition and distribution of the cycled Ca-20h anode in TOF-SIMS spectra. (c-f) Comparison of the element and fragments intensity of Ca-20h electrodes and Ca-20h electrodes after CV cycling. (g) TOF-MS data and fragments intensity evolution of the cycled Ca-20h surfaces.

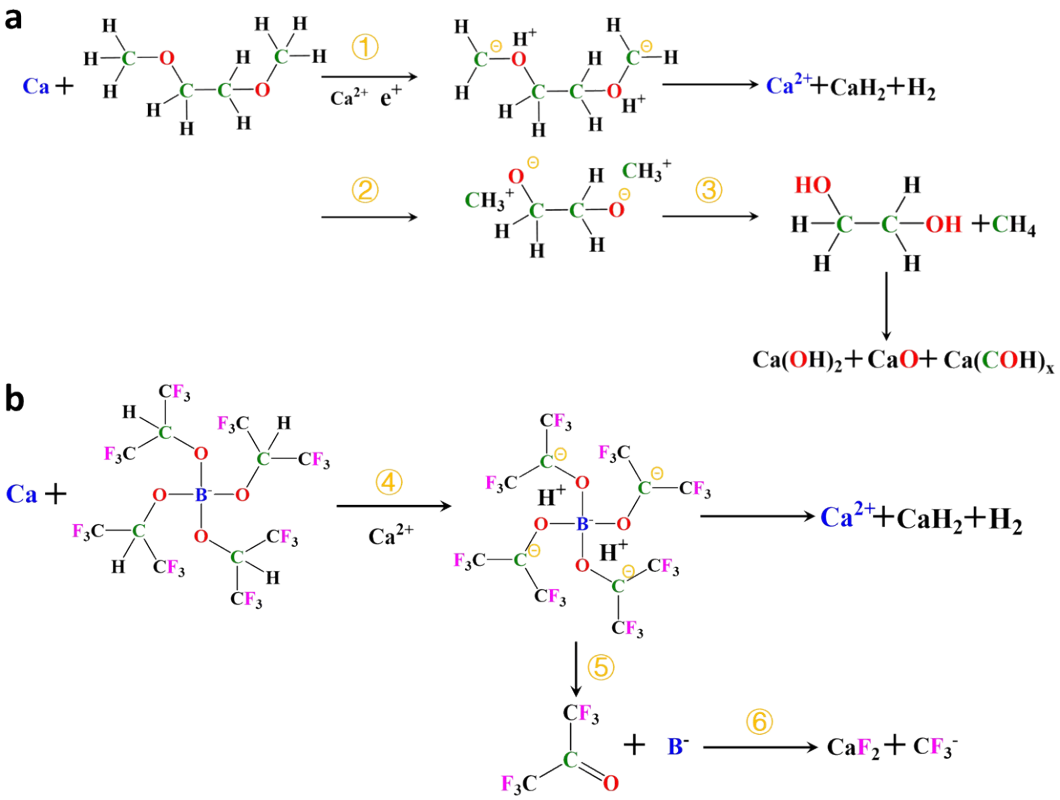

Figure S11. Proposed reaction mechanisms between Ca metal and $Ca[B(hfip)_4]_2$/DME electrolyte [4, 5]: (a) Possible reaction path between Ca metal and DME solvent to release H_2 and CH_4 gas. (b) the decomposition of $[B(hfip)_4]^-$ to release H_2 gas, in consistent with OEMS results in Figure 3a. The detailed procedures can be described as following:

(a) Reaction between Ca metal and DME:

① During Ca stripping (0 V→1 V), Ca^{2+} ions in electrolyte migrate to reduce the terminal proton (H^+) of the DME molecule to form H_2 and CaH_2.

② The O atom on the ether bond with an unshared electron pair can accept protons to form oxygen cation. The break of C-O bond can create alcohol groups (-OH) and CH_4.

③ The alcohol formed in ① reacts with Ca metal to get CaO, $Ca(OH)_2$, $(RO)_2Ca$ and other by products.

(b) Decomposition of $[B(hfip)_4]^-$ in assistance of Ca metal:

④ Ca^{2+} from electrolyte can reduce the terminal proton (H^+) of $[B(hfip)_4]^-$ anion to produce H_2 and CaH_2.

⑤ The O atom on the C-O-B bond has an unshared electron pair, which can accept protons and form oxygen cation. The B-O bond breaks, releasing a large number of B^-. The lone pair of carbanions on the C-O bond induces the formation of the C=O bond.

⑥The C-C bond at the end of C=O molecule is further broken to form CF_3^-, CaF_2.

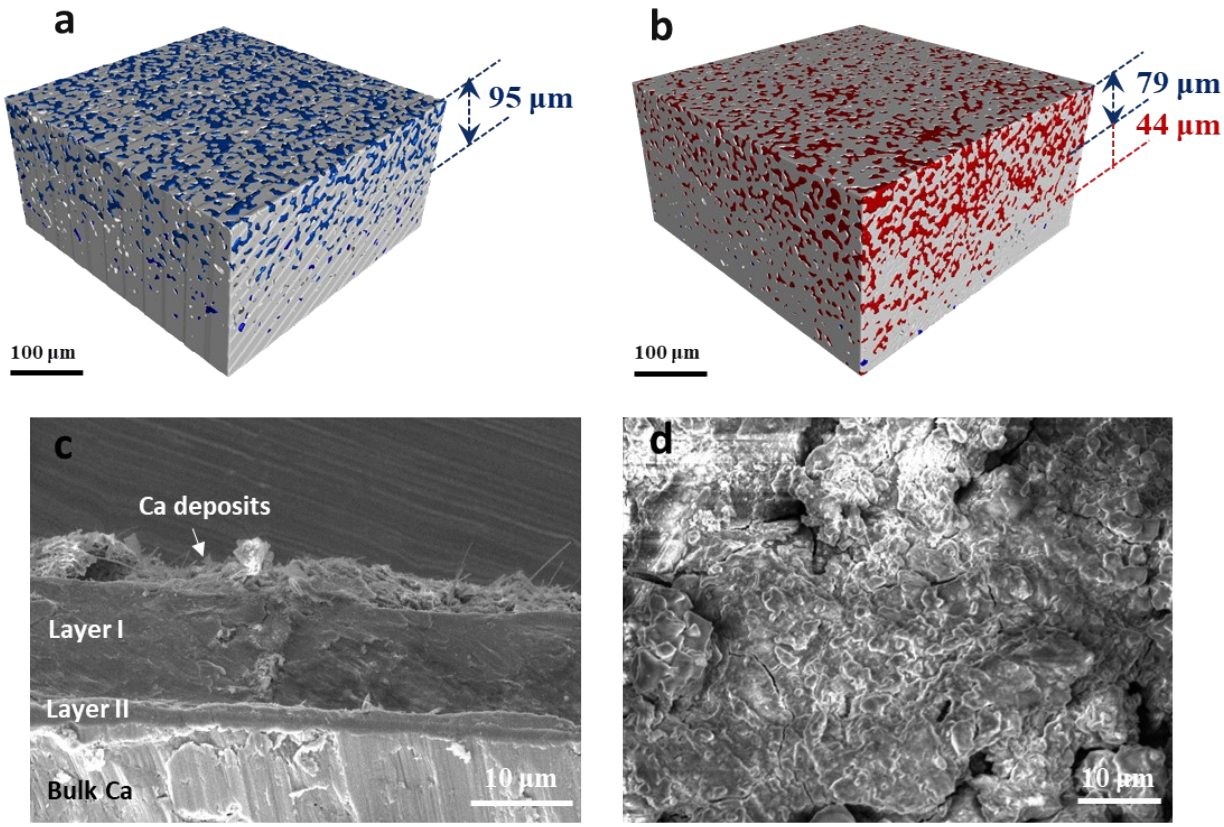

Figure S12. 3D nano-CT fragments analysis of Ca-20h electrodes (a) before and (b) after CV cycling. A porous passivating layer with a thickness of about 95 µm can be clearly identified for the Ca-20h electrode. Thickness of the porous passivating layer is increased to 123 µm for cycled Ca-20h electrode. The 3D-CT image of cycled Ca-20h shows two layers according to the pore size distribution, where the layer I (79 µm) exhibits larger pores and higher porosity than layer II (44 µm). (c) Cross sectional and (d) top-view SEM images of Ca-20h electrodes after 30 cycles under CV scanning. We can clearly observe the Ca deposits on the surface of the electrode, indicative of reversible Ca metal plating and stripping reactions. (c) also shows tri-layered structure including layer I (the native passivation layer), layer II (the secondary passivation layer) and bulk Ca metal underneath.

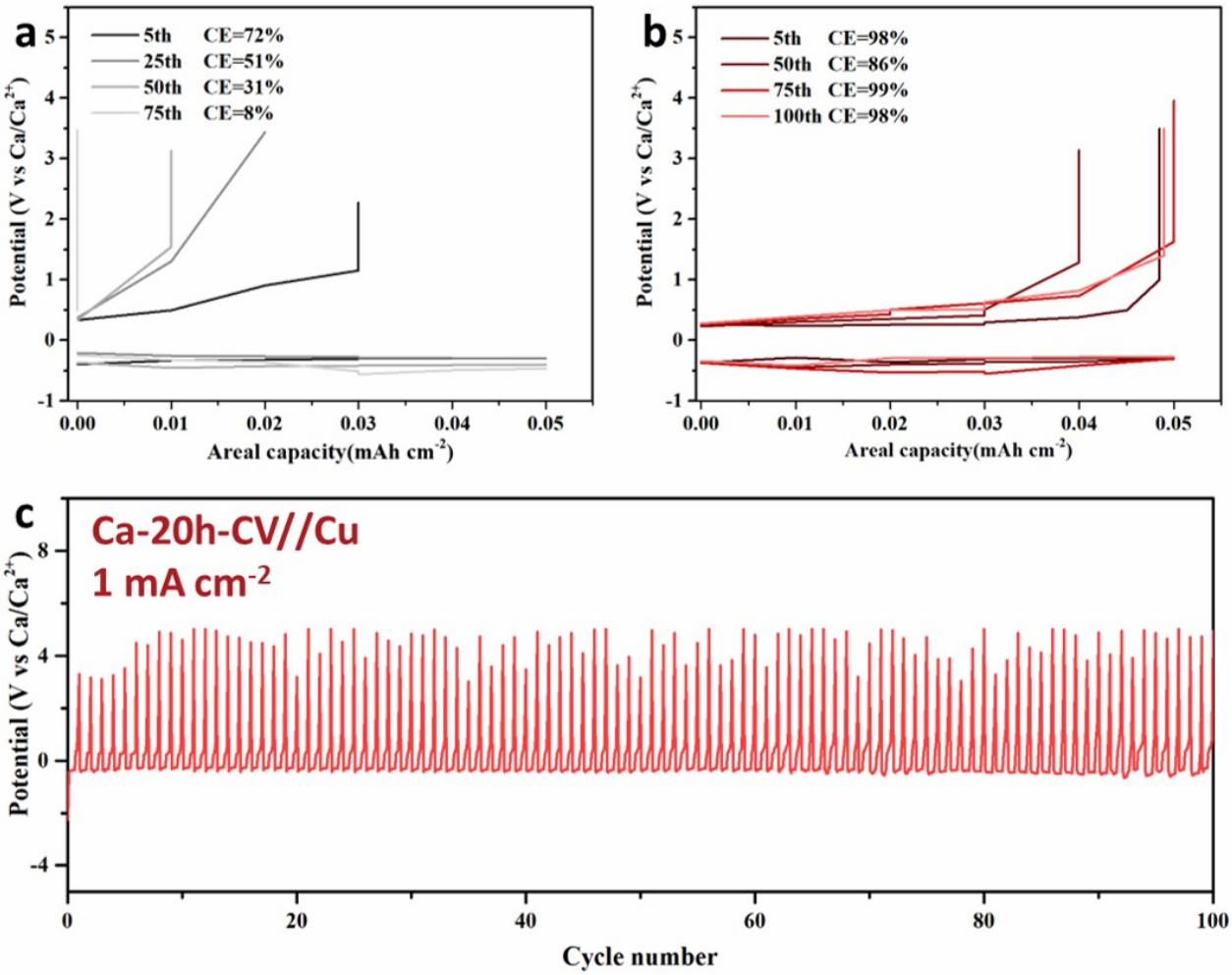

Figure S13. The representative voltage profiles and Coulombic efficiencies of (a) Ca//Cu and (b) Ca-20h-CV//Cu asymmetric cells in 0.25 M $Ca[B(hfip)_4]_2$/DME electrolyte cycling at a current density of 1 mA cm^{-2} and a deposition capacity of 0.05 mAh cm^{-2} per process. The Ca-20h-CV electrodes with pre-passivation layers deliver higher Coulombic efficiencies and lower overpotentials than pristine Ca metal electrodes. (c) The representative cyclic voltage profiles of Ca-20h-CV//Cu asymmetric cells.

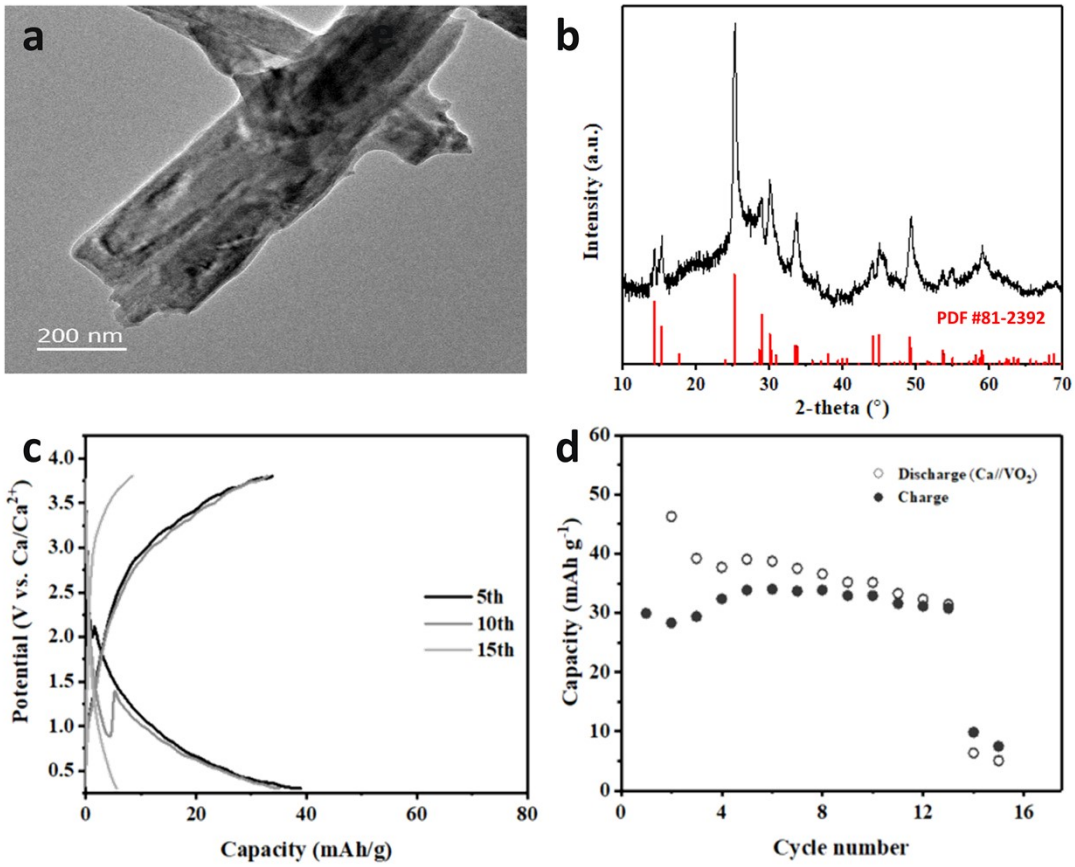

Figure S14. (a) TEM image and (b) XRD pattern of VO_2. (c) Charge–discharge voltage curves and (d) cyclic capacities of the pristine Ca//VO_2 full cells in 0.25 M $Ca[B(hfip)_4]_2$/DME electrolyte at 50 mA g^{-1}.

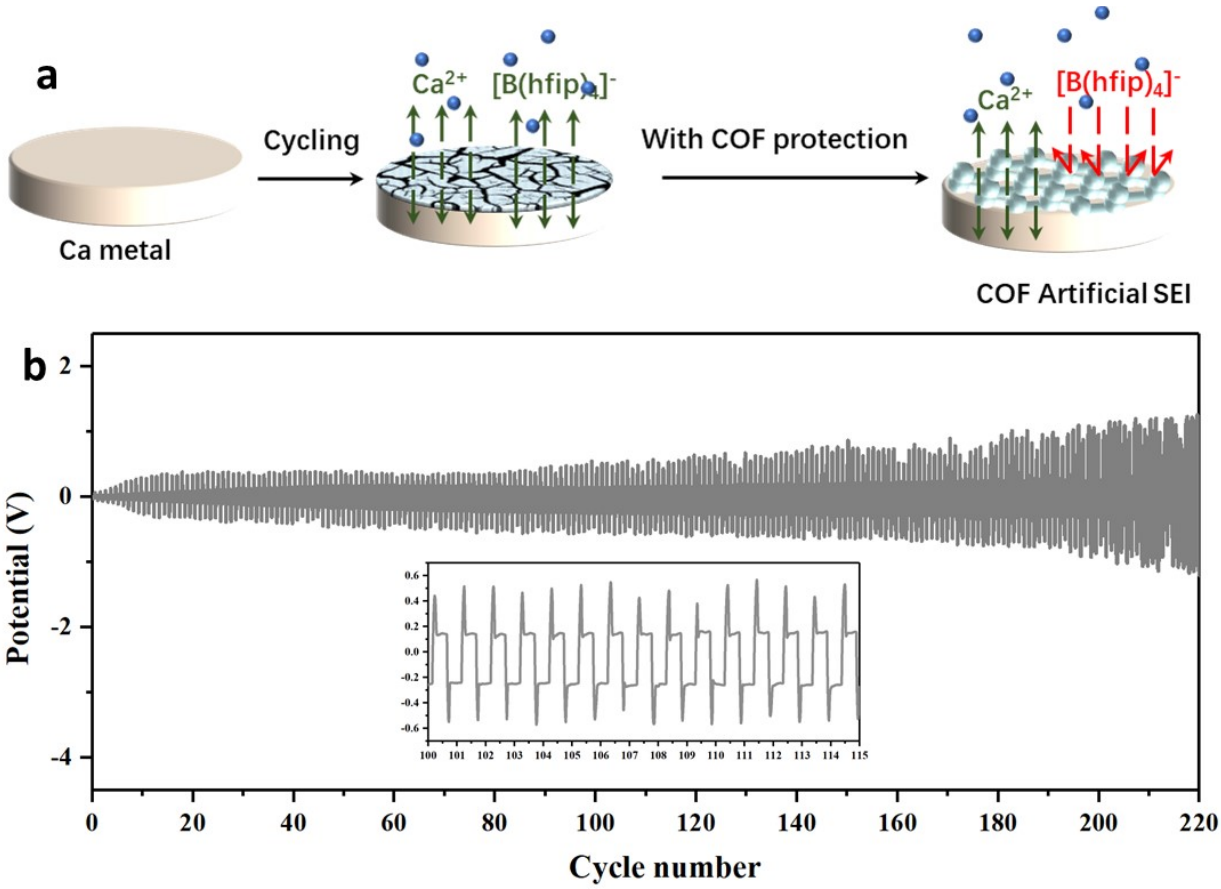

Figure S15. (a) Schematic images of using COF artificial SEI layers to protect Ca metal in $Ca[B(hifp)_4]_2$/DME electrolyte solutions (b) Voltage profiles of Ca symmetric cells using $TpPaSO_3Ca_{0.5}$ COF as artificial SEI layers cycling at 50 μA cm^{-2} for 220 cycles.

.

Reference：

[1] G. M. Hobold, K.-H. Kim and B. M. Gallant, *Energy Environ. Sci.*, 2023, **16**, 2247-2261.

[2] B. Zhou, I. Stosevski, A. Bonakdarpour and D. P. Wilkinson, *ACS Appl. Energy Mater.* 2023, **6**, 6890−6895.

[3] M. Srout, M. Carboni, J.-A. Gonzalez, and S. Trabesinger, *Small* 2023, **19**, 2206252.

[4] E. W. C. Spotte-Smith, T. B. Petrocelli, H. D. Patel, S. M. Blau and K. A. Persson, *ACS Energy Lett.* 2023, **8**, 347−355.

[5] X. Chen, L. Qin, J. Sun, S. Zhang, D. Xiao and Y. Wu *Angew. Chem*. *Int. Ed.* 2022, **134**, e202207.